

Radio spectral characteristics of the supernova remnant Puppis A and nearby sources

E. M. Reynoso¹★ and A. J. Walsh²★

¹*Instituto de Astronomía y Física del Espacio (IAFE), Av. Int. Güiraldes 2620, Pabellón IAFE, Ciudad Universitaria, Ciudad Autónoma de Buenos Aires, Argentina*

²*International Centre for Radio Astronomy Research, Curtin University, GPO Box U1987, Perth, WA 6845, Australia*

Accepted 2015 May 18. Received 2015 May 11; in original form 2015 March 20

ABSTRACT

This paper presents a new study of the spectral index distribution of the supernova remnant (SNR) Puppis A. The nature of field compact sources is also investigated according to the measured spectral indices. This work is based on new observations of Puppis A and its surroundings performed with the Australia Telescope Compact Array in two configurations using the Compact Array Broad-band Backend centred at 1.75 GHz. We find that the global spectral index of Puppis A is $\alpha = -0.563 \pm 0.013$. Local variations have been detected, however this global index represents well the bulk of the SNR. At the SE, we found a pattern of parallel strips with a flat spectrum compatible with small-scale filaments, although not correlated in detail. The easternmost filament agrees with the idea that the SNR shock front is interacting with an external cloud. There is no evidence of the previously suggested correlation between emissivity and spectral index. A number of compact features are proposed to be evolved clumps of ejecta based on their spectral indices, although dynamic measurements are needed to confirm this hypothesis. We estimate precise spectral indices for the five previously known field sources, two of which are found to be double (one of them, probably triple), and catalogue 40 new sources. In the light of these new determinations, the extragalactic nature previously accepted for some compact sources is now in doubt.

Key words: radiation mechanisms: non-thermal – techniques: interferometric – ISM: individual objects: Puppis A – ISM: supernova remnants – radio continuum: ISM.

1 INTRODUCTION

Puppis A is one of the most interesting supernova remnants (SNRs) in the Southern hemisphere. Its large extent (~ 50 arcmin in diameter) and high surface brightness provides an unparalleled chance to study detailed structures. Together with Cassiopeia A and G292.0+1.8, it is one of the three oxygen-rich Galactic SNRs, where fast oxygen knots of still uncontaminated ejecta have been detected at optical wavelengths (Winkler & Kirshner 1985) and in X-rays (Katsuda et al. 2008). Relative abundances of metal-rich ejecta measured on the NE portion are consistent with a progenitor with a mass in the range from 15 to 25 M_{\odot} (Hwang, Petre & Flanagan 2008; Katsuda et al. 2010).

The compact X-ray source RX J0822–4300, near the centre of the shell and hence dubbed ‘central compact object’ (CCO), has been identified as the stellar remnant left behind after the supernova (SN) outburst (Petre, Becker & Winkler 1996; Zavlin, Trümper & Pavlov 1999). The explosion site was spotted by Winkler et al.

(1988) through measuring proper motions of ejecta knots and filaments. This position is fully consistent with the direction of the CCO velocity (Hui & Becker 2006; Winkler & Petre 2007; Becker et al. 2012). Castelletti et al. (2006) propose that the CCO could be ejecting two opposite jets whose termination shocks appear in radio and X-rays as the eastern and western ‘ears’.

The age of Puppis A is estimated to vary between 3700 yr, based on the proper motion of optical filaments (Winkler et al. 1988), and 5200 yr, based on the velocity of the CCO and its projected distance to the explosion centre (Becker et al. 2012). The brightest, eastern rim of the shell is apparently interacting with a molecular cloud (Dubner & Arnal 1988; Reynoso et al. 1995; Paron et al. 2008), whose systemic velocity of $\sim +14$ km s⁻¹ translates into a kinematic distance of 2.2 kpc. However, Woermann, Gaylard & Otrupcek (2000) observed several pointings towards Puppis A and in the immediate vicinity in the four 18 cm lines of OH and concluded that the systemic velocity of the remnant is 7.6 km s⁻¹ rather than $+14$ km s⁻¹, which would bring the SNR about 1 kpc closer.

In X-rays, Puppis A is one of the brightest SNRs, and the emission is mostly dominated by shocked interstellar medium (ISM; Hwang, Flanagan & Petre 2005; Hwang et al. 2008; Dubner et al. 2013). Infrared (IR) observations carried out with the *Spitzer Space*

* E-mail: ereynoso@iafe.uba.ar (EMR); andrew.walsh@curtin.edu.au (AJW)

Telescope (Arendt et al. 2010) show an extremely good correlation with X-ray emission, indicating that the thermal IR emission mostly arises from swept-up dust collisionally heated by the hot, shocked plasma. Puppis A has also been detected in γ -rays between 0.2 and 100 GeV with the *Fermi* satellite (Hewitt et al. 2012), but not above 260 GeV (HESS Collaboration et al. 2015). The lack of emission at TeV energies implies that a spectral break or cutoff would occur at 280 or 450 GeV, depending upon the power law model assumed. A break or radiative cutoff are expected if the acceleration of particles after the collision with an external cloud has now ceased (HESS Collaboration et al. 2015).

Puppis A was widely observed at radio-continuum wavelengths, both with single dish telescopes (Milne & Hill 1969; Kundu 1970; Milne 1971; Milne, Stewart & Haynes 1993) and interferometers (Green 1971; Milne, Goss & Danziger 1983; Arendt et al. 1990; Dubner et al. 1991; Castelletti et al. 2006). Analysis of the polarized emission (Kundu 1970; Milne 1972; Dickel & Milne 1976; Milne et al. 1993) shows a predominantly radial magnetic field, low polarization, and little depolarization over most of the remnant. The first spectral index estimation of Puppis A was done by Milne & Hill (1969) who, based on the computed value of -0.5 , concluded that this radio source was an SNR. Subsequent studies refined the determination of the bulk spectral index as $\alpha = -0.52 \pm 0.03$ (Castelletti et al. 2006)¹ or $\alpha \simeq -0.53$ (Milne 1971; Dubner et al. 1991). High-resolution studies have unveiled that the spectral index varies spatially across the remnant (Dubner et al. 1991; Castelletti et al. 2006). In this paper, we revisit the spectral distribution of Puppis A applying a T-T plot method, which removes the problem of the zero level that can distort the results if the background emission is not properly accounted for. Our analysis is based on new wide band radio observations performed with the Compact Array Broad-band Backend (CABB) of the Australia Telescope Compact Array (ATCA). In addition, we re-analyse five previously known compact sources and list about 40 new compact sources in the field.

2 OBSERVATIONS AND DATA REDUCTION

Puppis A was observed simultaneously in the H I 21 cm line, in four OH 18 cm lines, and in radio-continuum with the CABB of the ATCA in two 13 hr runs. The first run took place on 2012 May 20 using the array configuration EW 352 (baselines varying from 31 to 352 m excluding the 6th antenna), and the second, on 2012 July 6 in the 750A configuration (baselines from 77 to 735 m). Including the 6th antenna adds baselines between 3015 and 3750 m for the 750A configuration, and between 4087 and 4439 for the EW 352 configuration. The primary flux and bandpass calibrator was PKS 1934–638, while PKS 0823–500 was used for phase calibration. Due to the large angular size of Puppis A, observations were made in mosaicking mode with 24 pointings in order to cover not only the SNR but also its surroundings. Following the Nyquist theorem, the pointings were separated by 19.6 arcmin to optimize the sampling at 1.4 GHz. The radio continuum was observed using a 2 GHz bandwidth divided into 2048 channels of 1 MHz width, centred at 1750 MHz. The analysis of the H I and OH lines will be developed in subsequent papers.

The data reduction was carried out with the MIRIAD software package (Sault, Teuben & Wright 1995). The uv data were split in bands of 128 MHz. For each band, calibrator and source observations were

inspected and flagged for interference and corrupted data. The standard data calibration routines were applied. We have not used the whole set of visibilities to construct a map because the presence of sources with very different spectral slopes within the observed field will introduce non-negligible errors due to bandwidth smearing in a frequency band as wide as 2 GHz. Therefore, we preferred to use at most three consecutive bands in a single image. Using a multi-frequency technique, we constructed an image at 1.4 GHz merging the bands centred at 1302, 1430 and 1558 MHz. The data were Fourier-transformed with uniform weighting to reduce sidelobes, and cleaned with MOSMEM. The resulting image, shown in Fig. 1, has a beam of 82.2×50.6 arcsec, with a position angle of $-0:55$, and a noise level of 1.5 mJy beam⁻¹, and is centred at 1395.6 MHz. A few residual sidelobe rings from the bright compact source at RA(2000) = $8^{\text{h}}20^{\text{m}}35^{\text{s}}.6$, Dec.(2000) = $-43^{\circ}0'23''$ could not be completely removed. The integrated flux density is computed to be 115 ± 8 Jy, where the error is dominated by the uncertainty in the background emission and the outermost contour level adopted. The agreement between this value and that reported by Castelletti et al. (2006) indicates that at this frequency the uv -coverage, combined with the mosaicking technique, samples all scale structures within Puppis A.

To compute spectral indices, we applied a standard T-T plot method (see Section 3.1). This method requires that the two images to be compared, one at each frequency, be obtained from visibilities within a same uv range and convolved with the same beam. The first condition ensures that both images sample features with similar scales. Adopting the first frequency to be 1.4 GHz and the second 2.5 GHz, visibilities were found to overlap in the range between 0.2 and 4 $\kappa\lambda$. We therefore constructed an additional image at 1.4 GHz following the same method as in Fig. 1 but using only this limited visibility range. The uv -filtered image thus obtained has a beam of 80.8×49.5 arcsec, with a position angle of $-0:4$. The image at 2.5 GHz was constructed merging the visibilities within the same uv range (0.2–4 $\kappa\lambda$) in the bands centred at 2326, 2454 and 2582 MHz. This image was convolved with the same beam as the uv -filtered image at 1.4 GHz. To enhance the compact sources reducing the diffuse emission, two more sets of maps were formed with more restrictive uv ranges, from 0.5 to 4 $\kappa\lambda$ and from 1 to 4 $\kappa\lambda$, respectively.

Finally, to perform an accurate analysis of the compact sources, an image was constructed for each band applying a more restrictive visibility range, from 0.8 to 4 $\kappa\lambda$, to filter out extended emission. These images were then used to compute flux densities and sizes, minimizing the uncertainties introduced by underlying background emission. The reduction in the number of visibilities due to the use of one single band and the restricted uv range results in a poor imaging and a higher noise, which makes the recognition of the weakest sources more difficult. Such sources were confirmed when they were detected in most frequency bands.

3 RESULTS

3.1 Spectral index computation

To compute spectral indices minimizing the uncertainty introduced by the always arbitrary selection of the zero level, we have applied a T-T plot technique. A description of this method, widely used over selected regions in extended radio sources (e.g. Costain 1960; Anderson & Rudnick 1993; Uyaniker et al. 2004; Leahy 2006; Reynoso & Green 2007), can be found in Turtle et al. (1962) and Reich & Reich (1988). Basically, the idea is to assume that the

¹ Note that, as an intermediate step in the data processing, Castelletti et al. (2006) used two flux densities, at 86 and 408 MHz, and found that $\alpha = -0.6$.

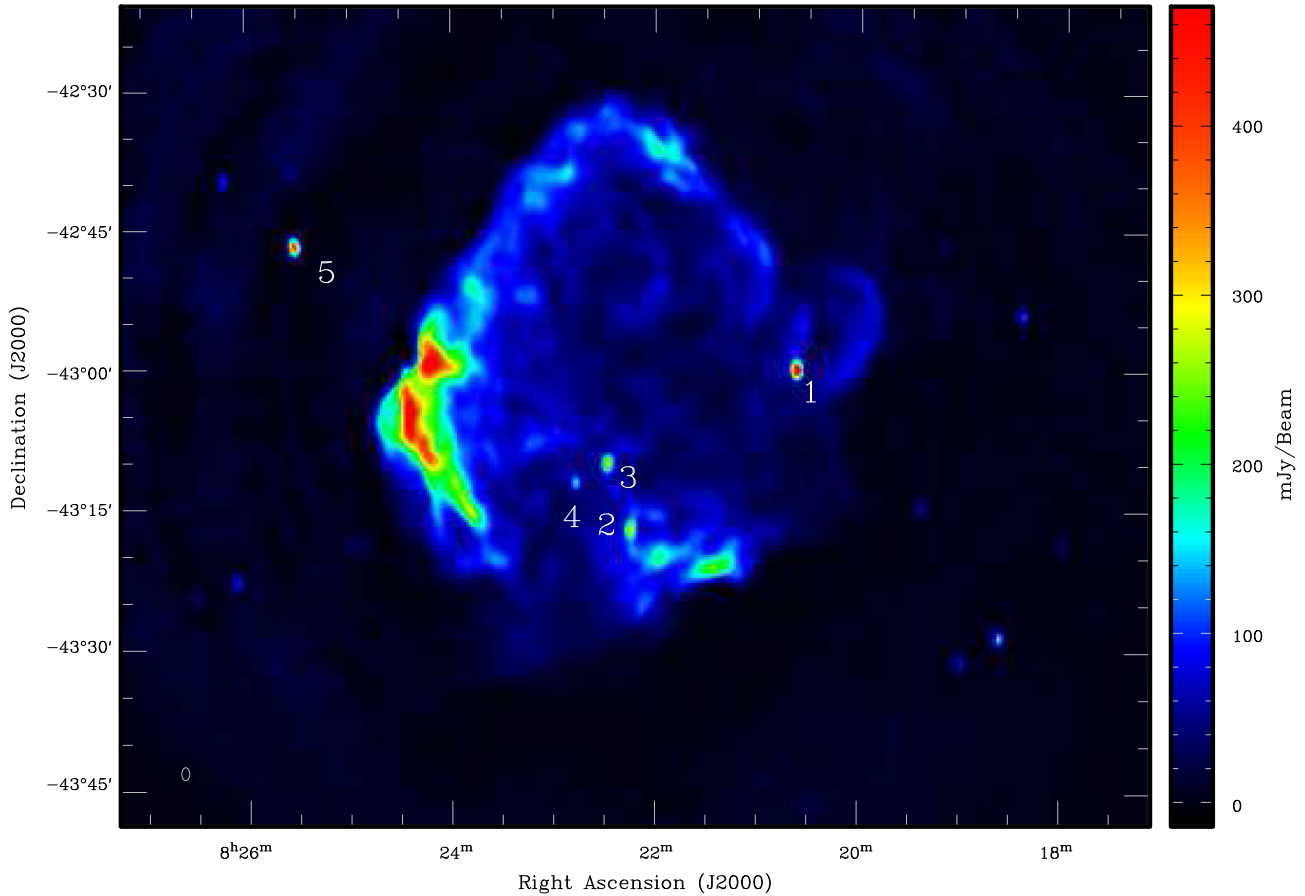


Figure 1. Image of Puppis A at 1.4 GHz. The beam size is 82.2×50.6 arcsec, with a position angle of $-0^\circ.55$. The flux density scale is shown at the right. The noise level is $1.5 \text{ mJy beam}^{-1}$. The beam is plotted at the bottom left corner. The white numbers 1 to 5 correspond to the compact sources discussed in Section 3.2.

observed continuum emission at a given frequency $T(\nu)$ can be written as $T(\nu) = T_s(\nu) + T_0(\nu)$, where $T_s(\nu)$ is the source emission and $T_0(\nu)$ is an isotropic background component, which includes an offset zero. Then, if $T_s(\nu) \propto \nu^\beta$ with β constant, the brightness temperature at two different frequencies are linearly related as

$$T(\nu_1) = T(\nu_2) \left(\frac{\nu_1}{\nu_2} \right)^\beta + C, \quad (1)$$

where $C = T_0(\nu_1) - T_0(\nu_2)(\nu_1/\nu_2)^\beta$. Thus, plotting $T(\nu_1)$ in terms of $T(\nu_2)$ for all pixels within a given region, the value of the brightness temperature spectral index β is readily obtained from the slope of the linear regression independently of the zero level of each of the two maps.

In what follows, we will refer to the flux density spectral index α defined by $S(\nu) \propto \nu^\alpha$, which is related to the brightness temperature spectral index as $\alpha = \beta + 2$. As the region where this method is applied becomes smaller, there is a better chance that both hypotheses, i.e. background isotropy and constant α , approach reality. A limitation of this technique, already pointed out by Anderson & Rudnick (1993), is that spectral indices can only be measured at scales compatible with the region analysed, while larger features are filtered out.

The quoted uncertainties correspond to the formal statistical errors of the linear regressions scaled by $\sqrt{(\text{beam area}/\text{pixel area})}$ (Green 1990). The scaling factor is due to the oversampling of the

images, otherwise the statistical errors in the linear fits may be underestimated since adjacent pixels are not independent and there are typically many pixels per beam (see for example Gaensler et al. 1999; Doherty et al. 2003). The quoted uncertainties, therefore, account for oversampling and contain possible small-scale variations of the local background emission. In this estimation, the contribution of the flux density noise levels of each frequency map has not been taken into account.

Although T-T plots are less accurate for extended sources, we used this method to estimate a global spectral index for Puppis A. We first plotted the uv -filtered image at 2.5 GHz in terms of the same at 1.4 GHz (Fig. 2). To avoid spurious contribution from emission unrelated to Puppis A, the brightest point sources projected within the SNR shell were removed in both images. The 1.4 and 2.5 GHz images were clipped at 15 and 10 mJy beam^{-1} , respectively. A linear fit yielded a spectral index of $\alpha = -0.573 \pm 0.004$, with a correlation coefficient of 0.9946. Inverting the frequencies, the result is $\alpha = -0.554 \pm 0.004$. Averaging both results, the global spectral index of Puppis A is $\alpha = -0.563 \pm 0.013$, where the error encloses the two values obtained above.

To map the spectral index distribution, we considered each pixel as the centre of a 7×7 pixel box and fitted a T-T plot over the box between 1.4 and 2.5 GHz. The box was slid in two dimensions over the SNR at 1 pixel increments. We adopted clip levels of 20 and 15 mJy beam^{-1} , respectively, and all linear fits where the correlation coefficients were lower than 0.950, or where the regression involved

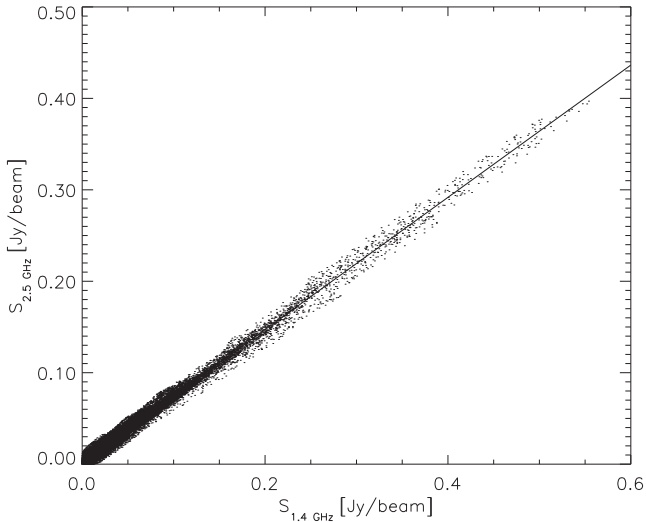


Figure 2. T-T plot between 1.4 and 2.5 GHz for the whole SNR Puppis A. Clip levels of 15 and 10 mJy beam⁻¹, respectively, were applied. Background sources were removed. The fit yields a spectral index of $\alpha = -0.573 \pm 0.004$.

less than 6 pixels, were blanked out. This procedure was repeated for $S_{2.5\text{ GHz}}$ against $S_{1.4\text{ GHz}}$ and vice versa, and the average between both maps was computed. The result is shown in Fig. 3. In good agreement with the global spectral index estimated through the T-T plot shown in Fig. 2, the average spectral index of Puppis A obtained over Fig. 3 after removal of the background sources gives

$\alpha = -0.59 \pm 0.22$, where the larger error is due to spatial variations of the synchrotron spectra.

3.2 Field compact sources

A number of compact sources, either projected within the SNR shell or in the surroundings, are present in our maps. However, only five of them have been reported in previous surveys (Day et al. 1972; Slee 1977; Milne et al. 1983; Dubner et al. 1991), four of them superimposed on the SNR face. In Fig. 1, these sources have been labelled with numbers increasing with Right Ascension (note that Milne et al. 1983, name them with letters A to E following the same ordering). According to Milne et al. (1983) and Dubner et al. (1991), sources 1 to 4 have spectral indices close to -1.0 , pointing to an extragalactic origin. Those indices are based on the direct comparison of integrated flux densities at two frequencies. Source 5, catalogued as 0823-426 by Slee (1977) and misidentified by Dubner et al. (1991) as their source 4, did not have enough information to accurately compute a spectral index (Milne et al. 1983). Moreover, it was observed at 80 and 160 MHz with the Culgoora radioheliograph (Slee 1977) but was not identified in the Parkes survey at 2.7 GHz (Day et al. 1972).

Here, we refine the calculation of the spectral indices for all five catalogued sources by two methods: T-T plots and a linear fit to the logarithmic plot S_ν versus ν , where ν is each of the frequencies in which the CABB data were divided, and S_ν is the flux density of the source. In the first case, we used the maps filtered with visibilities between 0.5 and 4 k λ (see Section 3.1), and averaged the spectral indices obtained by exchanging both frequencies alternately

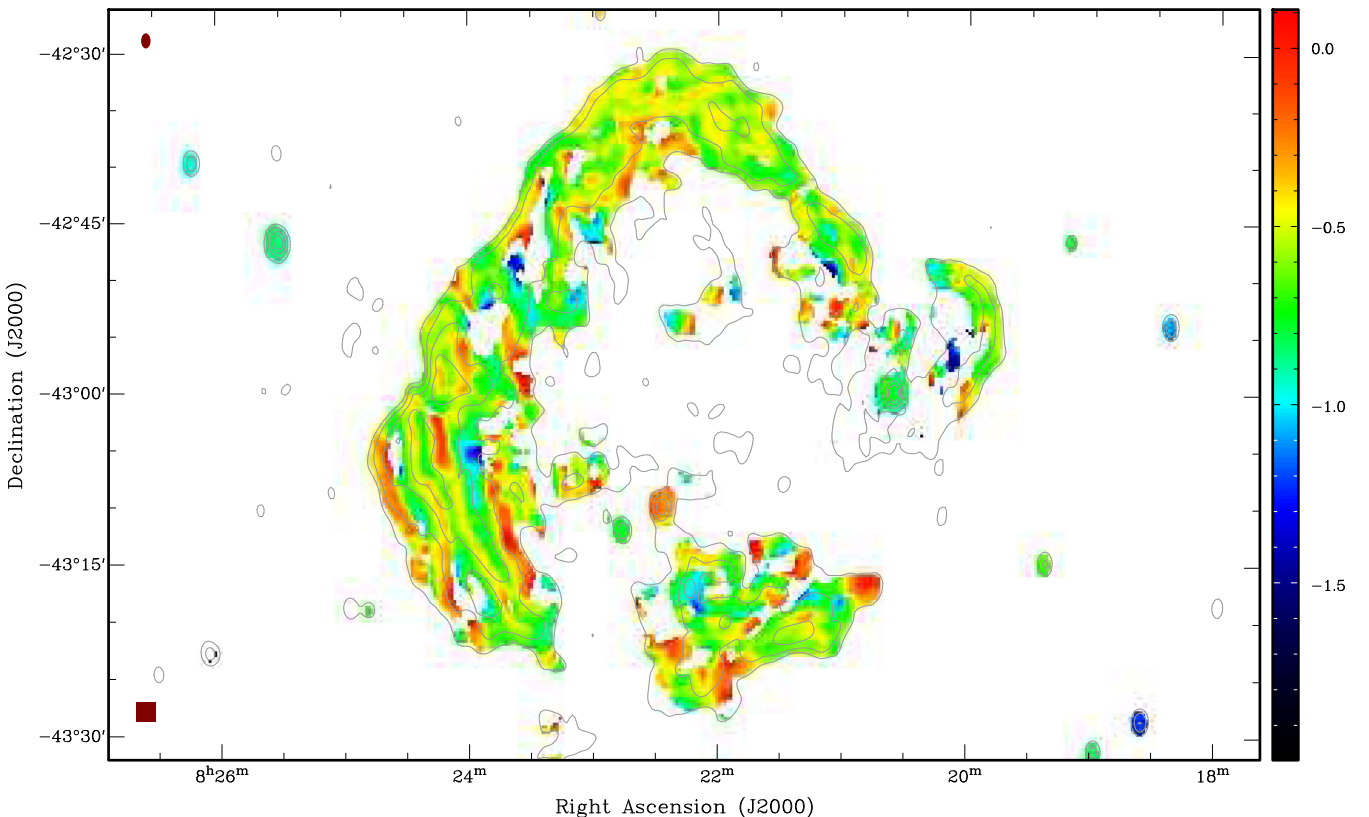


Figure 3. Spectral index distribution along Puppis A and surroundings. The filled box of 7×7 pixels at the bottom left corner represents the size of the area where T-T plots were computed. All pixels where the linear fits to the T-T plot had a correlation coefficient lower than 0.950 were blanked. The bar at the right displays the spectral index. Radio continuum 1.4 GHz contours at 20, 60, 150, 300 and 500 mJy beam⁻¹ are overlaid. The beam is shown at the top left corner.

Table 1. Catalogued compact sources.

Source number	RA (J2000) h m s	Dec. (J2000) ° ' "	Spectral index ^a	Spectral index ^b	Previous names
1	08 20 35.6	−43 00 23	$−0.76 ± 0.04$	$−0.86 ± 0.04$	G260.2−3.7 ⁽¹⁾
2	08 22 13.4	−43 17 38	$−0.91 ± 0.07$	$−1.09 ± 0.05$	
3	08 22 27.0	−43 10 29	$−0.26 ± 0.07$	$−0.56 ± 0.5$	ATPMN J082226.8−431026 ⁽²⁾ 2XMM J082226.9−431026 ⁽³⁾
4	08 22 45.7	−43 12 38	$−0.75 ± 0.15$	$−0.94 ± 0.08$	G260.7−3.7 ⁽¹⁾
5	08 25 30.7	−42 46 57	$−0.92 ± 0.04$	$−1.09 ± 0.09$	Cul 0823-426 ⁽⁴⁾

Notes. (1) Day, Caswell & Cooke (1972); (2) McConnell et al. (2012); (3) Watson et al. (2009); (4) Slee (1977).

^aT-T plot.

^bSlope of $S(\nu)$ versus ν .

as abscissa or ordinate. To apply the second method, flux densities were obtained over the images per individual band (as described in the last paragraph of Section 3.1) by fitting a two-dimensional Gaussian to each source and integrating the fitted function, allowing for a background level. To ensure the robustness of the fits, we made use of two image processing packages: MIRIAD and AIPS. Both results were in general agreement, and the error bars are consistent with the slight differences we measure between the results of these two packages.

In Table 1, we list all five sources and their spectral indices as measured with T-T plots (fourth column) and with the slope of the S_ν versus ν curve (fifth column). In all cases, the quoted errors correspond to the linear fits, regardless of the image sensitivity or other sources of uncertainty, like the limits of the integrated regions in the estimation of S_ν or the background level (we adopted the integrated flux density provided by the Gaussian fit over the source in each image). The plots and the corresponding fits are displayed in Fig. 4.

It is striking that T-T plots show a curvature for sources 3 and 4, with the highest flux density points departing from the fitted line. To illustrate this issue, we try different fits to the points and show the results in Fig. 5. The left-hand column displays images of sources 3 (top) and 4 (bottom) at 1.4 GHz constructed with visibilities between 0.5 and 4 $\kappa\lambda$. The right-hand column shows the corresponding T-T plots, where the solid lines coincide with the fits shown in Fig. 4, in which all flux densities above 45 and 35 mJy beam^{-1} at 1.4 and 2.5 GHz, respectively, for source 3, and above 30 and 20 mJy beam^{-1} at 1.4 and 2.5 GHz, respectively, for source 4, were taken into account. Limiting the range up to 100 and 80 mJy beam^{-1} at 1.4 and 2.5 GHz, respectively, for source 3, and up to 80 and 50 mJy beam^{-1} at 1.4 and 2.5 GHz, respectively, for source 4, the resulting spectral indices are $\alpha = -0.5 \pm 0.3$ for source 3, and $\alpha = -1.0 \pm 0.4$ for source 4. In Fig. 5, these fits are represented with a dashed line. If only the brightest core of each source is considered (fluxes above 150 and 120 mJy beam^{-1} at 1.4 and 2.5 GHz, respectively, for source 3, and above 80 and 50 mJy beam^{-1} at 1.4 and 2.5 GHz, respectively, for source 4), the resulting spectral indices are $\alpha = -0.14 \pm 0.20$ for source 3, and $\alpha = -0.55 \pm 0.35$ for source 4 (dotted lines in Fig. 5). For clarity, the parameters used for all the fits above and the corresponding spectral indices derived are summarized in Table 2. The curious behaviour depicted by these two sources implies that there is a gradient of spectral indices from the centre (flatter) to the edges (steeper).

For completeness, in Table 3 we list all new compact sources detected in the field with a flux density above 10 mJy at 1.3 GHz, estimated on the single 128 MHz band image (see last paragraph of Section 3.1). These sources are numbered following Table 1, ordered

with increasing Right Ascension. In the fourth column, we give the integrated flux density at 1.3 GHz. As in the previously catalogued sources, a 2D-Gaussian fit was applied to each source, allowing for an offset, and the flux density is computed by integrating the fitted distribution. We also include a spectral index estimation based on T-T plots obtained as in Table 1 for those sources for which the correlation coefficient of the linear fit is better than 0.95.

4 DISCUSSION

The energy distribution of an SNR contains information on the mechanisms involved in particle acceleration processes. Spectra produced by shock-accelerated radio-synchrotron-emitting electrons typically have a spectral index $\alpha \simeq -0.6$ (e.g. Bietenholz, Kassim & Weiler 2001). In the test-particle limit, adiabatic shocks have a theoretical spectral index $\alpha = -0.5$, assuming a compression ratio $r = 4$ in a monoatomic gas ($\gamma = 5/3$; e.g. Reynolds 2001). In radiative shocks, the test-particle limit is no longer valid as accelerated particles influence the shock dynamics, and can increase the compression ratio and produce flatter spectra. Fig. 6 displays the distribution of spectral indices as obtained from the Catalogue of Galactic Supernova Remnants compiled by Green (2014). Although the catalogue lists 294 sources, 135 of them have variable spectral indices, or an undetermined value (quoted value followed by a question mark). In Fig. 6, only the remaining 159 SNRs are considered. Spectral indices as extreme as 0.0 or -0.9 are marginally attained, but most SNRs have $-0.6 \lesssim \alpha \lesssim -0.4$. Spectral indices can also be altered by contamination with thermal Bremsstrahlung emission, interaction of the shock front with a denser medium or high energetic particles injected by an interior pulsar.

The most recent determination of the radio spectral index of Puppis A has been carried out by Castelletti et al. (2006) who combine a number of flux densities corresponding to frequencies between 19 and 8400 MHz, and obtain $\alpha = -0.52 \pm 0.03$. Although in agreement within the error limits, this value is somewhat flatter than the value inferred here from the T-T plot (Fig. 2). However, we notice that there appears to be a flattening near 10–100 MHz (fig. 4 in Castelletti et al. 2006), where the observational points do not follow the fitted single power law model. If the two fluxes at the lowest frequencies are excluded, then $\alpha = -0.56 \pm 0.04$, in excellent agreement with our result.

Extended SNRs such as Puppis A provide a unique chance to analyse local variations of the spectral index, which may reflect local changes in the particle acceleration mechanisms. In general, regions of diffuse emission have steeper spectra (e.g. Cygnus Loop; Uyaniker et al. 2004). As an extreme case, S147 has a global spectral index of -0.3 but in selected diffuse regions it varies between -1.1

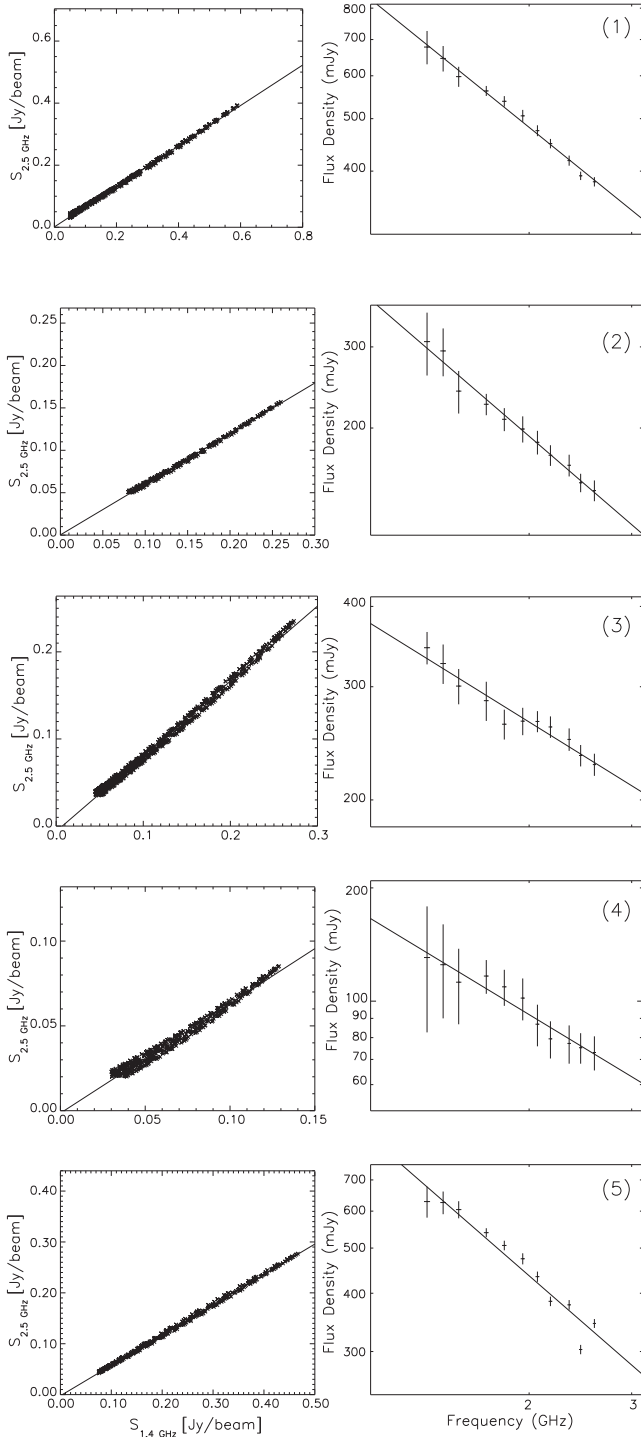


Figure 4. For each of the five previously known sources, T-T plots (left-hand column) and the corresponding linear fits to the flux densities $S(\nu)$ in terms of frequency (right-hand column). The numbers at the top right corner of each frame in the right-hand column correspond to the number assigned to each source in Table 1 and in Fig. 1.

and -1.56 (Xiao et al. 2008). The difference between the spectral indices for bright filaments and diffuse regions in S147 is reflected in the two branches where the points gather in the T-T plots. In Puppis A, in contrast, all points in the T-T plot can be fitted by a single line (Fig. 2), which means that this SNR is well represented

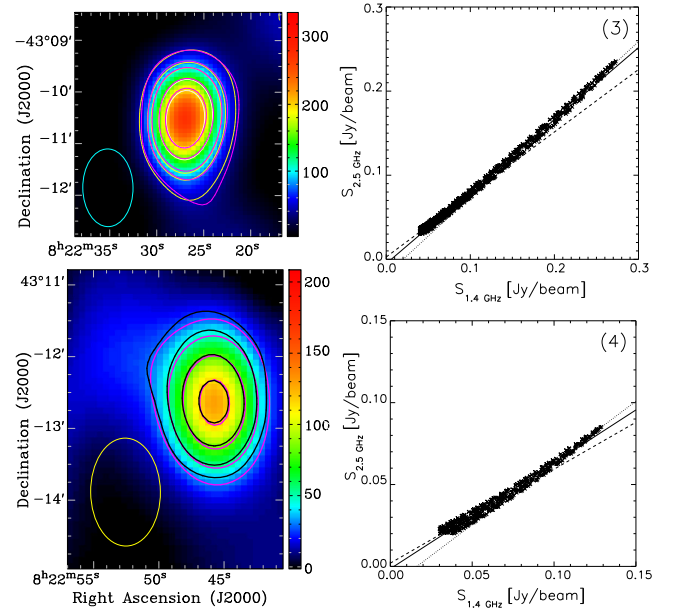


Figure 5. Top, left-hand panel: compact source 3 at 1.4 GHz. The beam is plotted at the bottom left corner. Black contours (yellow in the online colour version) at 45, 80, 100, 150 and 200 mJy beam $^{-1}$ are overlaid to represent the emission at 1.4 GHz, while grey (magenta) contours correspond to the emission levels 35, 60, 80, 120 and 160 mJy beam $^{-1}$ at 2.5 GHz. The flux density scale, in units of mJy beam $^{-1}$, is shown at the right. Top, right-hand panel: T-T plot for source 3 with the same fit as in Fig. 4 (solid line) and using different flux density ranges (see text). Bottom, left-hand panel: compact source 4 at 1.4 GHz. The beam is plotted at the bottom left corner. Grey (magenta) contours at 30, 50, 80 and 115 mJy beam $^{-1}$ are overlaid to represent the emission at 1.4 GHz, while white (black) contours correspond to the emission levels 20, 30, 50 and 75 mJy beam $^{-1}$ at 2.5 GHz. The flux density scale, in units of mJy beam $^{-1}$, is shown at the right. Bottom, right-hand panel: T-T plot for source 4 with the same fit as in Fig. 4 (solid line) and using different flux density ranges (see text).

Table 2. Spectral variations for sources 3 and 4.

	Flux density range at 1.4 GHz (mJy)	Flux density range at 2.5 GHz (mJy)	Spectral index
3	$S \geq 45$	$S \geq 35$	-0.26 ± 0.06
	$45 \leq S \leq 100$	$35 \leq S \leq 80$	-0.5 ± 0.3
	$S \geq 150$	$S \geq 120$	-0.14 ± 0.20
4	$S \geq 30$	$S \geq 20$	-0.7 ± 0.2
	$30 \leq S \leq 80$	$20 \leq S \leq 50$	-1.0 ± 0.4
	$S \geq 80$	$S \geq 50$	-0.55 ± 0.35

by a unique global spectral index. Nevertheless, spatial variations are observed, which will be analysed in the following section.

4.1 Spatial spectral index variations

The first study of the spatial distribution of spectral indices in Puppis A was performed by Dubner et al. (1991). They compare two images, at 327 and 1515 MHz, obtained with the Karl G. Jansky Very Large Array (VLA) and integrate the emission in a few boxes over relevant areas. They find that the eastern region is considerably steeper than the southern, western, northern and central regions, with $\alpha = -0.67 \pm 0.08$.

Table 3. New compact sources.

	RA (J2000) h m s	Dec. (J2000) ° ' "	$S_{1.3\text{GHz}}^a$ mJy	Spectral index
6	08 17 58.6	-43 18 37	53.5 ± 8.5	
7	08 18 22.6	-42 54 12.5	133 ± 7	-1.25 ± 0.07
8	08 18 35.3	-43 28 47.0	180 ± 10	-1.17 ± 0.08
9	08 18 42	-42 53 03	20 ± 6	-0.5 ± 0.4
10	08 18 57.9	-43 31 29.5	90 ± 7	-0.78 ± 0.08
11	08 19 11	-42 46 55	46 ± 6	-0.75 ± 0.25
12	08 19 18.5	-43 23 55	10 ± 3.5	
13	08 19 22.2	-43 15 09	76.5 ± 7.5	-0.70 ± 0.15
14	08 19 35	-43 39 03	17.5 ± 7.5	
15	08 19 49	-43 24 40	14 ± 4	-0.1 ± 0.3
16	08 19 58	-43 50 50.3	49 ± 6	
17	08 20 25	-43 47 11	12 ± 6	
18	08 20 40	-42 09 14	29 ± 4	
19	08 20 51	-42 24 00	18 ± 6	-0.74 ± 0.30
20	08 21 09	-43 22 35.4	46 ± 3	
21	08 21 22	-42 16 19	40 ± 6	-1.12 ± 0.25
22	08 21 42	-42 31 43	33 ± 8	-1.0 ± 0.4
23	08 21 51	-43 48 37	35 ± 6	
24	08 22 20	-43 51 24	18 ± 6	
25	08 22 38	-42 30 19	29 ± 4	-0.70 ± 0.45
26	08 22 56	-42 26 55	36 ± 6	-0.35 ± 0.45
27	08 24 27	-43 00 24	85 ± 15	
28	08 24 48	-43 19 24	26 ± 5	-0.53 ± 0.45
29	08 24 57	-43 19 17.3	37 ± 5	-0.6 ± 0.3
30	08 25 05	-43 09 21	12 ± 8	
31	08 25 06	-42 42 19	12 ± 5	
32	08 25 31	-42 39 09	27 ± 6	-0.8 ± 0.4
33	08 25 40	-43 10 36	15 ± 4	
34	08 25 40	-43 31 29	18 ± 8	
35	08 25 53	-43 24 14	15 ± 5	
36	08 26 05	-43 22 59.4	100 ± 5	-1.3 ± 0.5
37	08 26 11.7	-42 39 53.3	127 ± 8	-0.9 ± 0.1
38	08 26 30	-43 24 43	41 ± 5	

^aThe flux density at 1.3 GHz is estimated on the single 128 MHz band image (see last paragraph of Section 3.1).

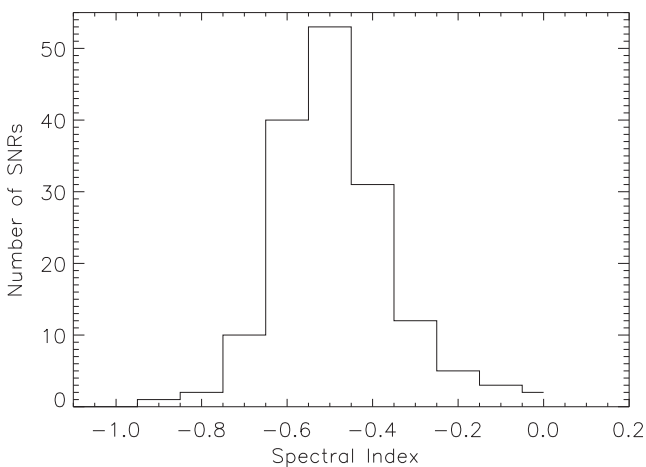


Figure 6. Distribution of the spectral indices of catalogued Galactic SNRs (Green 2014). Only 159 out of the 294 catalogued SNRs were considered, after discarding variable or unconfirmed spectral indices.

More recently, Castelletti et al. (2006) improved the analysis by combining new observations at 1425 MHz undertaken with the VLA with the old 327 MHz data re-processed from scratch. To ensure that all scale structures are sampled, they integrate single dish observations in their maps. They apply two techniques to survey the spectral index distribution. The first method divides directly the logarithm of the ratios between fluxes and frequencies:

$$\alpha = \frac{\ln \left(\frac{S_{\nu_1}}{S_{\nu_2}} \right)}{\ln \left(\frac{\nu_1}{\nu_2} \right)}. \quad (2)$$

The second method, called ‘tomography’, consists of scaling one of the images by a test spectral index α_t and subtracting it from the other frequency image. The resulting images, $S_t = S_{\nu_1} - \left(\frac{\nu_1}{\nu_2} \right)^{\alpha_t} S_{\nu_2}$, will be closer to zero as the test spectral index approaches the real one, and features with different spectral indices will be highlighted as light (positive) or dark (negative) as their spectra are steeper or flatter than the assumed α_t . In contrast to Dubner et al. (1991), Castelletti et al. (2006) point out that the bright eastern features are somewhat flatter than the rest of the shell.

Both methods are sensitive to offsets in the background emission. In particular, to include the large-scale emission at 327 MHz, Castelletti et al. (2006) use single dish archival data at 408 MHz and scale it with a spectral index $\alpha = -0.6$ derived from two images, at 86 MHz (Mills, Slee & Hill 1960) and at 408 MHz (Green 1971). Therefore, the subsequent analysis can be influenced to some extent by this assumed uniform spectral index. Here, we apply a third method which is independent of the background emission level and does not use archival observations or pre-determined results. The method, described in detail in Section 3.1, is called ‘T-T plots’, and the spectral index distribution is shown in Fig. 3. We first call to attention that this method does not provide information on the spectral index of the interior diffuse emission, since the uv -filtering performed to construct the maps from a same spatial frequency range in the Fourier domain, filters out the underlying large-scale emission. Besides, the size of the region adopted to compute the fit sets an additional limit to the scale to which this method is sensitive, since only spectral indices associated with small-scale features whose brightness vary significantly within the region can be measured (Anderson & Rudnick 1993).

To compare our results with previous studies of spectral index distribution, we also calculated T-T plots for the regions shown in Fig. 7. For the southern region (bottom panel), the T-T plot for the area enclosed by the outermost contour, within the selected box, yields $\alpha = -0.66 \pm 0.20$, steeper than the value reported by Dubner et al. (1991). The inner peak has a steeper spectrum: $\alpha = -0.8 \pm 0.4$, in agreement with the tomographic image in Castelletti et al. (2006) for $\alpha_t = -0.8$, in which most of Puppis A has vanished but the southern peak is still visible. The western ear-like feature (top, right-hand panel), for which Dubner et al. (1991) estimated a spectral index of -0.56 , could not be reliably fitted: we found $\alpha = -0.6$, but with a very poor correlation coefficient (lower than 0.75). The low emission at this region, close to the rms level, must be a reason for the increase of the noise of the T-T plot. Besides, as Castelletti et al. (2006) noticed, this feature has a combination of different structures with variable spectral indices (see also Fig. 3).

The eastern region (top, left-hand panel in Fig. 7) has a global spectral index of $\alpha = -0.6 \pm 0.1$ when the emission included in the outermost contour for the whole map is considered. This value is in agreement with Dubner et al. (1991) within the error margins. If the individual boxes are taken separately, the results are:

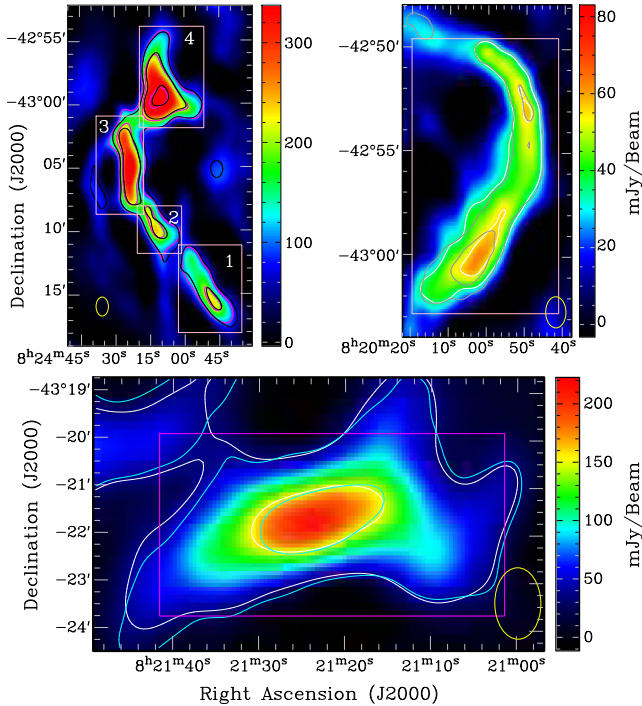


Figure 7. Radio images of selected regions of Puppis A (top, left-hand panel: eastern region; top, right-hand panel: western ear-like feature; bottom: southern region) at 1.4 GHz using visibilities within the spatial frequency range from 0.5 to 4 $k\lambda$. The beam is shown at the bottom left corner. Representative contours at 1.4 and 2.5 GHz are overlaid, together with the boxes on which the T-T plots were calculated.

$\alpha_{\text{box 1}} = -0.60 \pm 0.45$, $\alpha_{\text{box 2}} = -0.64 \pm 0.35$, $\alpha_{\text{box 3}} = -0.68 \pm 0.25$ and $\alpha_{\text{box 4}} = -0.55 \pm 0.12$. Curiously, when the T-T plots are limited to the brightest regions, the result is different for boxes 3 and 4: for the first one, the spectrum steepens ($\alpha = -0.8 \pm 0.4$), while for the latter, it gets flatter ($\alpha = -0.50 \pm 0.35$). This means that the synchrotron emission and the radio spectral behaviour are not necessarily correlated.

In the spectral index map presented in Fig. 3, T-T plots were computed on boxes of $\sim 100 \times 100$ arcsec, which is more than twice the beam area. In most cases, regions where the spectral indices are more extreme (black and white in Fig. 3, or blue and red in the online colour version) are correlated with the larger errors in the spectral index determination ($\Delta\alpha \simeq 0.6$). However, the uncertainties of the flat spectrum filaments at the south-eastern region are low enough to ensure their reliability. Our results do not reproduce the striation found by Castelletti et al. (2006) along the shell, with fringes perpendicular to the Declination axis. Instead, as mentioned above, Fig. 3 shows a pattern of narrow strips at the south-eastern region parallel to the rim which is not correlated with the emission observed in the radio maps (Fig. 1 and uv -filtered images for T-T plots). To explore the nature of these filaments, in Fig. 8 we show an image of Puppis A constructed from a more restrictive uv range, with visibilities from 1 to 4 $k\lambda$, in which extended structures are further removed. The eastern region depicts a number of bright filaments whose general appearance resembles the pattern observed in the spectral index distribution, suggesting that the variations in α are connected with structures at this scale. The fact that they do not share a detailed correlation, as noticed also by Castelletti et al. (2006) in Puppis A and by Anderson & Rudnick (1993) in the SNRs G39.2–0.3 and G41.1–0.3, probably means that the varia-

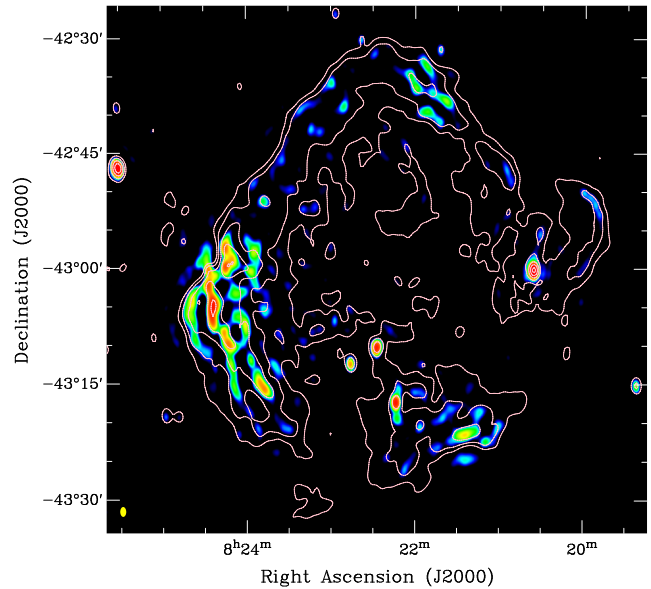


Figure 8. Radio image of Puppis A at 1.4 GHz using visibilities within the spatial frequency range from 1 to 4 $k\lambda$. The beam is shown at the bottom left corner. To enhance bright features, the intensity is displayed with a logarithmic scale. Contours are as in Fig. 3.

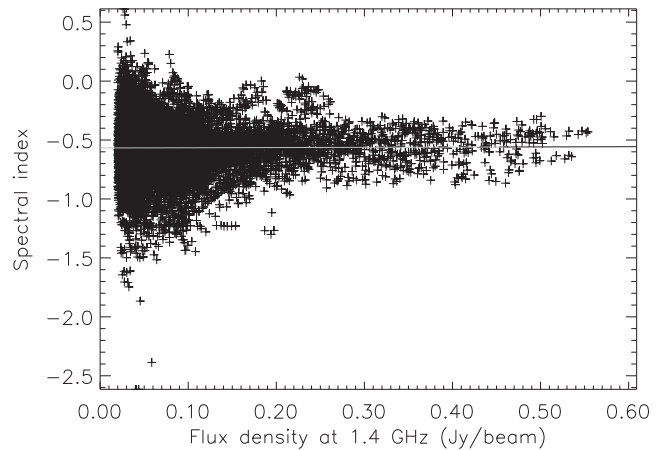


Figure 9. Spectral index versus flux density at 1.4 GHz for Puppis A. Compact sources have been removed. The solid line represents a linear fit for flux densities above 20 mJy beam^{-1} .

tions in spectral index are due to aspects of the hydrodynamic flow unrelated with synchrotron emissivity. Besides, if the spectrum of the electron population is intrinsically bent, different degrees of compression can result in spectral index variations (Anderson & Rudnick 1993).

Anderson & Rudnick (1993) mention that in old shell SNRs, the higher emissivity parts are flatter than the fainter or diffuse parts of the remnants (e.g. Fuerst & Reich 1986; Uyaniker et al. 2004; Ingallinera et al. 2014), while in younger SNRs like Puppis A, the brighter regions apparently tend to be associated with steeper indices. To see if there is evidence of any such trend, in Fig. 9 we plot the spectral index against the flux density of Puppis A at 1.4 GHz after removing the compact sources. For flux densities above 20 mJy beam^{-1} , the distribution is fit by an almost horizontal

line, with a slope of 0.018 ± 0.026 . The average spectral index is -0.57 ± 0.05 , with no variations along the flux density axis. This result confirms that there is no obvious correlation between emissivity and spectral index.

Flatter spectra are interpreted as sites of active particle acceleration (Anderson & Rudnick 1996). As a shock front encounters gas at a higher density and lower temperature, the Mach number increases and the spectrum flattens (Anderson & Rudnick 1993; Leahy & Tian 2005). In Fig. 3, it is clear that the filament at the easternmost part of the shell has a flatter spectrum than the rest of the rim. This is consistent with the presence of an external cloud interacting with Puppis A, as suggested by several atomic and molecular line studies (Dubner & Arnal 1988; Reynoso et al. 1995; Paron et al. 2008). In other SNRs, shocked clumps are not found to be associated with flat spectral indices (e.g. HB21; Leahy 2006); this is probably because any interaction with a denser gas must be followed by important ionization losses for the spectrum to flatten.

Castelletti et al. (2006) suggest that the eastern and western ‘ears’ observed in radio and X-rays could be the termination shocks of two opposite jets ejected by the CCO. The spectral index distribution of these features does not offer any hint to help conclude if this scenario is true, since the eastern ear is clearly flatter than the western one. A possible explanation for the difference in α if both features share the same origin, would be that the eastern shock has encountered a denser ISM and the flatter spectral index is due to this interaction.

4.2 Compact sources

Previous high-resolution radio surveys of Puppis A (Milne et al. 1983; Dubner et al. 1991; Castelletti et al. 2006) have reported the presence of four compact sources superimposed on the SNR face,² listed as sources 1 to 4 in Table 1. Source 3 is the only one with an X-ray counterpart (Dubner et al. 2013). Milne et al. (1983) estimate spectral indices for these four sources comparing their observations at 21 cm with the Molongo map at 408 MHz (Green 1971) and find $\alpha \simeq -1.0$ for all of them. Dubner et al. (1991) compare flux densities at 327 and 1515 MHz and find spectra steeper than -1.0 for all but source 3, for which $\alpha = -0.8$. Based on the tomographic image for a test spectral index of -0.8 , Castelletti et al. (2006) conclude that all four sources are steeper than -0.8 and, therefore, extragalactic. Our results do not confirm these results except for source 2, which is clearly extragalactic, together with source 5 which lacks previous estimations of the spectral index. However, the results are more in line if we note that source 3 does not appear anymore in the tomographic image of Castelletti et al. (2006) with $\alpha_t = -0.8$ (hence the spectral index is limited between $-0.8 < \alpha < -0.6$), and source 4 is marginally observed, which means that $\alpha \simeq -0.8$ but not steeper.

From Table 1, spectral indices measured from the curve $S(\nu)$ versus ν are systematically steeper than those derived using T-T plots. For sources 1 and 4, the steeper indices would not be in conflict with previous results. However, spectral indices obtained with the T-T plot method are more reliable, since they are free of the following problems involved with flux estimates. In the first place, splitting the uv data into 128 MHz bands has the disadvantage that the reduced number of visibilities per band increases the noise level of the images and makes the removal of sidelobes more challenging.

² A Molonglo contour map at 408 MHz (Green 1971) shows all four sources, but only the brightest one (source 1) is identified as an unresolved source with a spectrum steeper than the rest of Puppis A.

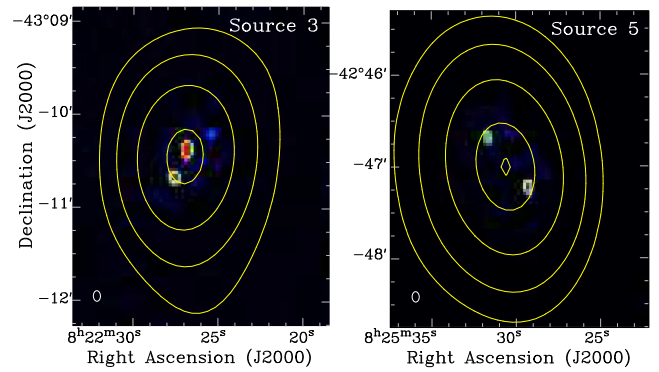


Figure 10. Left: very high resolution (HPBW = 6.8×4.6 arcsec) image of source 3 at 1.4 GHz. The beam is indicated in the bottom left corner. Contours of an image at 1.4 GHz filtered in uv between 0.2 and 4 $k\lambda$ (Section 2) are overlaid, at 40, 80, 150 and 250 mJy beam^{-1} . Right: same as left for source 5, where the plotted contours are 30, 80, 200, 400 and 500 mJy beam^{-1} .

And secondly, if the 2D Gaussian or offset fits are poor, the integrated flux density may not be accurate. The departure of several measured points from the fitted lines in the right-hand column of Fig. 4 can be ascribed to these two problems. In the case of sources 3 and 4, we have discussed in Section 3.2 that α varies from the core to the edges. When the core is excluded, the spectral indices derived from T-T plots and by fitting a line to $S(\nu)$ versus ν are coincident (compare Tables 1 and 2). This means that the contribution from the core is negligible when computing the total fluxes of these sources.

It is possible that the difference between the values of α measured here and in earlier works can be explained because sources 1–4 are superimposed on the diffuse component of Puppis A, and previous flux density determinations are probably contaminated with this background emission. It is also likely that one or more of these sources are variable. As an example, we notice that there is a difference of about a factor of 2 between the flux densities of sources 1 and 2 at 21 cm (500 and 230 mJy , respectively; Milne et al. 1983) and at 1515 MHz (230 and 160 mJy , respectively; Dubner et al. 1991), whereas according to the quoted spectral indices the difference should be less than 10 per cent. In that sense, the present work exhibits the unique advantage of being based on simultaneous observations.

Finally, we have made use of the visibilities associated with the 6th antenna of the ATCA, which vary in the range between 8 and 24 $k\lambda$, to construct very high resolution images (HPBW = 6.8×4.6 arcsec) of the brightest sources. These images reveal that sources 3 and 5 are double, as shown in Fig. 10, where the former could be even triple (a weaker feature probably real appears at the NW of the two brighter components). Such double-lobed structures are typical of extragalactic sources. The multiple nature of source 3 could explain the different spectral indices from the edge to the centre. However, source 4 does not show any structure on small scales, hence the reason of its spectral behaviour remains a mystery. Although previously identified as an extragalactic source, it is more likely a Galactic source that may even be associated with Puppis A.

Among the new compact sources catalogued in Table 3, double sources are also: 10, 21, 22, 25, 26 and 38, while source 36 is probably triple. Unfortunately, the uv sampling obtained with baselines that include only the 6th antenna is too scarce to perform a deeper investigation into the properties of these sources. New observations

with the ATCA in its 6 km configurations are desirable to uncover the nature of these multiple sources.

4.3 Ejecta ‘bullets’ in Puppis A?

There is plenty of evidence that core-collapse SN eject ‘bullets’ of stellar material (e.g. Wang & Chevalier 2002). These clumps evolve from an initial bow-shock phase to an instability stage, where Rayleigh–Taylor (R-T) fingers are developed along the forward face (Anderson et al. 1994). The high-velocity optical O-rich knots detected in Cassiopeia A (van den Bergh 1971) and G292.0+1.8 (Ghavamian, Hughes & Williams 2005) are SN ejected clumps in the early bow-shock phase. At more evolved stages, R-T fingers stretch and amplify the local magnetic field, and the clumps become bright radio-synchrotron emitters. Compact radio knots are observed in the young SNR Cassiopeia A (Anderson et al. 1994) and in the older Vela SNR (Duncan et al. 1996). In Cas A, radio knots have typical spectral indices around -0.75 independently of the knot velocity, and at the outer boundaries of the shell, spectra are even steeper ($\alpha \simeq -0.85$; Anderson et al. 1994). In Vela, several radio knots are the counterparts of high-velocity X-ray features (Strom et al. 1995; Duncan et al. 1996).

Castelletti et al. (2006) observed the presence of a compact feature (size ~ 45 arcsec) to the east, close to an intense X-ray region known as the ‘bright eastern knot’ (BEK; Petre et al. 1982; Hwang et al. 2005). They conclude that this source is extragalactic based on a spectrum steeper than -0.8 inferred from the tomographic images. In fact, this source is hardly observed in their tomographic image traced with $\alpha_t = -0.8$, which means that the spectral index is limited between $-0.8 < \alpha < -0.6$. We analysed our images filtered with visibilities between 1 and 4 k λ (Fig. 8) and could locate this source at RA(2000) = 8^h24^m13^s.9, Dec.(2000) = $-42^\circ 59' 55''$. The source is resolved, and its size is about 86×42 arcsec after deconvolving the fitted Gaussian by the beam. A T-T plot yields $\alpha = -0.8 \pm 1.1$. Thus, not only is the proposed extragalactic nature of this source not unequivocal, but the spectral index is compatible with a radio knot, like those found in Cas A.

Remarkably, this compact radio feature is located next to the BEK. Hwang et al. (2005) interpreted the X-ray emission from the BEK as coming from a shocked interstellar cloud based on the ‘voided sphere’ morphology similar to that produced in experimental simulations of interaction between shock waves and dense clouds. However, a molecular study failed to detect any gas concentration associated with the BEK (Paron et al. 2008). It should not be discarded that both the BEK and the radio source reported by Castelletti et al. (2006) are evolved ejecta bullets like those detected in X-rays and radio wavelengths in other SNRs. Moreover, the co-existence of ejecta clumps in their earlier stages (as optical O-rich knots) and in their more evolved phase (as radio knots) in Cas A suggests that radio knots can also be found in Puppis A, since both remnants share the characteristic system of O-rich high-velocity clumps ejected in the SN event.

We have searched for radio knots along the shell and found six more candidates, based on their spectral indices, which are displayed in Table 4. We also list five compact sources with spectra steeper than -1 , hence probably of extragalactic origin (although the error margins make their classification not conclusive), and two compact sources with a flat spectrum. Higher resolution and sensitivity images of these radio knot candidates will help to measure changes in intensity and position, and to unveil if they are individual clumps or are composed by a cluster of knots. Proper motion studies are crucial to conclude if these features are high-velocity ejecta.

Table 4. Radio knot candidates^a.

RA (J2000) h m s	Dec. (J2000) ° ' "	Spectral index
08 21 38.3	-42 38 22	-0.8 ± 0.5
08 21 51.4	-42 39 51	-0.7 ± 0.7
08 22 12.5	-43 19 36	-0.6 ± 1.1
08 22 50.4	-42 39 09	-0.8 ± 0.9
08 23 18.7	-42 52 34	-0.8 ± 1.1
08 24 12.4	-43 09 58	-0.6 ± 1.0
08 24 13.9	-42 59 55	-0.8 ± 1.1
08 21 42.2	-42 41 09	-1.3 ± 0.6
08 22 59.4	-42 36 06	-1.1 ± 0.3
08 23 07.7	-42 42 24	-1.3 ± 0.5
08 23 14.1	-42 41 56	-1.2 ± 1.2
08 23 47.3	-42 51 33	-1.2 ± 1.6
08 21 56.0	-43 20 51	-0.2 ± 0.7
08 23 56.37	-43 12 09	-0.35 ± 0.60

^aRadio knot candidates are listed in the upper band. For completeness, sources probably extragalactic found in the search are included in the central band, and flat spectrum sources, in the lower band.

5 CONCLUSIONS

Using the ATCA, we have imaged the prominent SNR Puppis A in continuum emission between 1 and 3 GHz. The observations included full 12 hr synthesis imaging in two arrays – EW 352 and 750 A. Our images are composed of 24 mosaic pointings and cover an area approximately 2×2 deg². The resultant data are of high sensitivity (1.5 mJy beam⁻¹) and high resolution ($\sim 80 \times 50$ arcsec).

We have used T-T plots to calculate the spectral index across Puppis A and derive a value of -0.563 ± 0.013 . Although local variations in the spectral index are noted, this global spectral index appears to well represent most of the SNR. Contrary to previous suggestions, we find no correlation between spectral indices and radio brightness. We identify filamentary structure, particularly in the eastern edge of the SNR, which resembles the pattern followed by the spectral index variations. This pattern was not detected in previous studies. We suggest that the outermost filament may be the result of interaction of the SNR with an external cloud. There is no evidence, based on the spectral index, of the eastern and western ‘ears’ being termination shocks of two opposite jets from the CCO. We also found a number of compact features that could be radio knots resulting from the evolution of clumpy SN ejecta. A dynamical study should clarify this hypothesis.

We investigate the nature of a number of compact sources that are found projected both within and outside of the SNR. Some of these compact sources do show strongly negative spectral indices, which are indicative of extragalactic sources. It is not clear that sources 1, 3 and 4 are extragalactic, as claimed in previous works. With the highest spatial resolution available to us, we are able to identify double-lobed structures in sources 3 and 5, confirming the extragalactic nature of the latter and suggesting the same for the former in spite of its flat spectral index. However, source 4, which was previously identified as extragalactic, shows a flatter spectral index with a radial gradient (like source 3) and does not show any structure on small scales. We therefore expect that source 4 is more likely a Galactic source that may well be associated with the SNR.

ACKNOWLEDGEMENTS

We thank the referee (Luke Bozzetto) for helpful and constructive criticism, which has improved the quality of this paper. We appreciate useful discussions with Laura Richter, Timothy Shimwell and Mark Wieringa for solving problems during data reduction. This research was partially funded by CONICET grants PIP 114-200801-00428 and 112-201207-00226. The Australia Telescope Compact Array is part of the Australia Telescope National Facility which is funded by the Commonwealth of Australia for operation as a National Facility managed by CSIRO. EMR is member of the Carrera del Investigador Científico of CONICET, Argentina.

REFERENCES

- Anderson M. C., Rudnick L., 1993, *ApJ*, 408, 514
 Anderson M. C., Rudnick L., 1996, *ApJ*, 456, 234
 Anderson M. C., Jones T. W., Rudnick L., Tregillis I. L., Kang H., 1994, *ApJ*, 421, L31
 Arendt R. G., Dwek E., Petre R., Dickel J. R., Roger R. S., Milne D. K., Kesteven M. J., 1990, *ApJ*, 350, 266
 Arendt R. G. et al., 2010, *ApJ*, 725, 585
 Becker W., Prinz T., Winkler P. F., Petre R., 2012, *ApJ*, 755, 141
 Bietenholz M. F., Kassim N. E., Weiler K. W., 2001, *ApJ*, 560, 772
 Castelletti G., Dubner G., Golap K., Goss W. M., 2006, *A&A*, 459, 535
 Costain C. H., 1960, *MNRAS*, 120, 248
 Day G. A., Caswell J. L., Cooke D. J., 1972, *Aust. J. Phys. Astrophys. Suppl.*, 25, 1
 Dickel J. R., Milne D. K., 1976, *Aust. J. Phys.*, 29, 435
 Doherty M., Johnston S., Green A. J., Roberts M. S. E., Romani R. W., Gaensler B. M., Crawford F., 2003, *MNRAS*, 339, 1048
 Dubner G. M., Arnal E. M., 1988, *A&AS*, 75, 363
 Dubner G. M., Braun R., Winkler P. F., Goss W. M., 1991, *AJ*, 101, 1466
 Dubner G., Loiseau N., Rodríguez-Pascual P., Smith M. J. S., Giacani E., Castelletti G., 2013, *A&A*, 555, A9
 Duncan A. R., Stewart R. T., Haynes R. F., Jones K. L., 1996, *MNRAS*, 280, 252
 Fuerst E., Reich W., 1986, *A&A*, 163, 185
 Gaensler B. M., Brazier K. T. S., Manchester R. N., Johnston S., Green A. J., 1999, *MNRAS*, 305, 724
 Ghavamian P., Hughes J. P., Williams T. B., 2005, *ApJ*, 635, 365
 Green A. J., 1971, *Aust. J. Phys.*, 24, 773
 Green D. A., 1990, *AJ*, 100, 1927
 Green D. A., 2014, *Bull. Astron. Soc. India*, 42, 47
 HESS Collaboration et al., 2015, *A&A*, 575, A81
 Hewitt J. W., Grondin M.-H., Lemoine-Goumard M., Reposeur T., Ballet J., Tanaka T., 2012, *ApJ*, 759, 89
 Hui C. Y., Becker W., 2006, *A&A*, 457, L33
 Hwang U., Flanagan K. A., Petre R., 2005, *ApJ*, 635, 355
 Hwang U., Petre R., Flanagan K. A., 2008, *ApJ*, 676, 378
 Ingallinera A., Trigilio C., Umana G., Leto P., Agliozzo C., Buemi C., 2014, *MNRAS*, 445, 4507
 Katsuda S., Mori K., Tsunemi H., Park S., Hwang U., Burrows D. N., Hughes J. P., Slane P. O., 2008, *ApJ*, 678, 297
 Katsuda S., Hwang U., Petre R., Park S., Mori K., Tsunemi H., 2010, *ApJ*, 714, 1725
 Kundu M. R., 1970, *ApJ*, 162, 17
 Leahy D. A., 2006, *ApJ*, 647, 1125
 Leahy D., Tian W., 2005, *A&A*, 440, 929
 McConnell D., Sadler E. M., Murphy T., Ekers R. D., 2012, *MNRAS*, 422, 1527
 Mills B. Y., Slee O. B., Hill E. R., 1960, *Aust. J. Phys.*, 13, 676
 Milne D. K., 1971, *Aust. J. Phys.*, 24, 429
 Milne D. K., 1972, *Aust. J. Phys.*, 25, 307
 Milne D. K., Hill E. R., 1969, *Aust. J. Phys.*, 22, 211
 Milne D. K., Goss W. M., Danziger I. J., 1983, *MNRAS*, 204, 237
 Milne D. K., Stewart R. T., Haynes R. F., 1993, *MNRAS*, 261, 366
 Paron S., Dubner G., Reynoso E., Rubio M., 2008, *A&A*, 480, 439
 Petre R., Kriss G. A., Winkler P. F., Canizares C. R., 1982, *ApJ*, 258, 22
 Petre R., Becker C. M., Winkler P. F., 1996, *ApJ*, 465, L43
 Reich P., Reich W., 1988, *A&AS*, 74, 7
 Reynolds S. P., 2001, *Space Sci. Rev.*, 99, 177
 Reynoso E. M., Green A. J., 2007, *MNRAS*, 375, 92
 Reynoso E. M., Dubner G. M., Goss W. M., Arnal E. M., 1995, *AJ*, 110, 318
 Sault R. J., Teuben P. J., Wright M. C. H., 1995, in Shaw R. A., Payne H. E., Hayes J. J. E., eds, *ASP Conf. Ser. Vol. 77, Astronomical Data Analysis Software and Systems IV, A Retrospective View of MIRIAD*. Astron. Soc. Pac., San Francisco, p. 433
 Slee O. B., 1977, *Aust. J. Phys. Astrophys. Suppl.*, 43, 1
 Strom R., Johnston H. M., Verbunt F., Aschenbach B., 1995, *Nature*, 373, 590
 Turtle A. J., Pugh J. F., Kenderdine S., Pauliny-Toth I. I. K., 1962, *MNRAS*, 124, 297
 Uyaniker B., Reich W., Yar A., Fürst E., 2004, *A&A*, 426, 909
 van den Bergh S., 1971, *ApJ*, 165, 457
 Wang C.-Y., Chevalier R. A., 2002, *ApJ*, 574, 155
 Watson M. G. et al., 2009, *A&A*, 493, 339
 Winkler P. F., Kirshner R. P., 1985, *ApJ*, 299, 981
 Winkler P. F., Petre R., 2007, *ApJ*, 670, 635
 Winkler P. F., Tuttle J. H., Kirshner R. P., Irwin M. J., 1988, in Roger R. S., Landecker T. L., eds, *IAU Colloq. 101: Supernova Remnants and the Interstellar Medium Kinematics of Oxygen-Rich Filaments in Puppis a*. Cambridge Univ. Press, Cambridge, p. 65
 Woermann B., Gaylard M. J., Otrupcek R., 2000, *MNRAS*, 317, 421
 Xiao L., Fürst E., Reich W., Han J. L., 2008, *A&A*, 482, 783
 Zavlin V. E., Trümper J., Pavlov G. G., 1999, *ApJ*, 525, 959

This paper has been typeset from a $\text{\TeX}/\text{\LaTeX}$ file prepared by the author.